

## Evaluating impact of detector arrangement and position resolution effect on a fast neutron-based range verification system for proton therapy

Setterdahl, Lena M.; Lionheart, William R.B.; Lathouwers, Danny; Ratliff, Hunter N.; Skjerdal, Kyrre; Meric, Ilker

**DOI**

[10.1016/j.radphyschem.2025.112793](https://doi.org/10.1016/j.radphyschem.2025.112793)

**Publication date**

2025

**Document Version**

Final published version

**Published in**

Radiation Physics and Chemistry

**Citation (APA)**

Setterdahl, L. M., Lionheart, W. R. B., Lathouwers, D., Ratliff, H. N., Skjerdal, K., & Meric, I. (2025). Evaluating impact of detector arrangement and position resolution effect on a fast neutron-based range verification system for proton therapy. *Radiation Physics and Chemistry*, 234, Article 112793. <https://doi.org/10.1016/j.radphyschem.2025.112793>

**Important note**

To cite this publication, please use the final published version (if applicable). Please check the document version above.

**Copyright**

Other than for strictly personal use, it is not permitted to download, forward or distribute the text or part of it, without the consent of the author(s) and/or copyright holder(s), unless the work is under an open content license such as Creative Commons.

**Takedown policy**

Please contact us and provide details if you believe this document breaches copyrights. We will remove access to the work immediately and investigate your claim.



Contents lists available at ScienceDirect

## Radiation Physics and Chemistry

journal homepage: [www.elsevier.com/locate/radphyschem](http://www.elsevier.com/locate/radphyschem)

## Evaluating impact of detector arrangement and position resolution effect on a fast neutron-based range verification system for proton therapy

Lena M. Setterdahl <sup>a</sup>, <sup>\*</sup>, William R.B. Lionheart <sup>b</sup>, Danny Lathouwers <sup>c</sup>, Hunter N. Ratliff <sup>a</sup>, Kyrre Skjerdal <sup>a</sup>, Ilker Meric <sup>a</sup><sup>a</sup> Department of Computer science, Electrical engineering and Mathematical sciences, Western Norway University of Applied Sciences, Inndalsveien 28, Bergen, 5063, Norway<sup>b</sup> Department of Radiation Science and Technology, Delft University of Technology, Mekelweg 15, Delft, 2629 JB, Netherlands<sup>c</sup> Department of Mathematics, University of Manchester, Alan Turing Building, Manchester, M13 9PL, United Kingdom

## ARTICLE INFO

## Keywords:

Proton therapy range verification  
Fast neutron imaging  
Organic scintillators  
Monte Carlo simulation

## ABSTRACT

Real-time proton therapy range verification is a technique that can potentially reduce uncertainty margins around the treatment volume and enable prompt corrections during treatment, making proton therapy a safer cancer treatment modality. Imaging secondary particles resulting from proton-beam nuclear interactions with tissue serves as a means of range verification. The NOVO project recently (2023) presented a compact detector array (NOVCoDA) range verification system designed to image secondary prompt-gamma rays (PGs) and fast neutrons (FNs). The position resolution and arrangement of detector elements within the NOVCoDA influences the reconstructed particle distributions and in turn the system's range shift detection capabilities. Through Monte-Carlo simulations, we investigate the effects of four different detector element arrangements and the utilization of optically segmented scintillator volumes within detector elements, for improved position resolution, on NOVCoDA's range shift determination capability for proton therapy. We limit our study to the detection of FNs produced by an 85-MeV proton beam interacting within a homogeneous water phantom. Results indicate that a parallel array with detector elements oriented perpendicular to the proton beam axis and line-of-sight direction yields the highest double FN scattering efficiency, on order of  $10^{-6}$  per proton. Furthermore, optically segmented detector elements resulted in improved minimum detectable range shift, reducing required proton intensity by 30%–60% to discern a 1 mm shift.

## 1. Introduction

Proton therapy is an increasingly used cancer treatment, having been administered to nearly 350,000 patients worldwide as of 2022 (Particle Therapy Co-Operative Group (PTCOG), 2022). Its growing use is largely due to its advantageous dose deposition characteristics, which enable highly precise treatments and better sparing of surrounding healthy tissues. However, the significant concentration of the dose at the Bragg peak makes proton therapy particularly vulnerable to deviations from the treatment plan or inherent uncertainties within the plan itself which may arise from anatomical and density changes, patient motion and uncertainties associated with estimating proton stopping power from computed tomography (CT) Hounsfield Units (Paganetti, 2012).

The current approach to mitigate these uncertainties is robust treatment planning, which explicitly accounts for potential errors in patient

positioning and proton range to minimize dosimetric variations (Yock et al., 2019). While this ensures that the prescribed dose is delivered to the clinical target volume (CTV) in the considered error scenarios, it comes at the expense of exposing surrounding healthy tissue to an additional dose (Fredriksson et al., 2011; Petit et al., 2013) in addition to limiting the choice of beam angles (Tattenberg et al., 2022, 2021). Minimizing range uncertainties would enhance precision and decrease exposure of normal tissue in proton therapy. In light of this, significant efforts have been directed toward creating instruments for verifying the proton range *in vivo* during, or after therapy. Non-invasive techniques rely on observing secondary particles produced during treatment which bear information on the proton beam range.

Particle-therapy Positron Emission Tomography (PET), developed in 1990, was proposed for imaging coincident 511 keV photon pairs

\* Corresponding author.

E-mail addresses: [Lena.Marie.Setterdahl@hvl.no](mailto:Lena.Marie.Setterdahl@hvl.no) (L.M. Setterdahl), [bill.lionheart@manchester.ac.uk](mailto:bill.lionheart@manchester.ac.uk) (W.R.B. Lionheart), [D.Lathouwers@tudelft.nl](mailto:D.Lathouwers@tudelft.nl) (D. Lathouwers), [Hunter.Nathaniel.Ratliff@hvl.no](mailto:Hunter.Nathaniel.Ratliff@hvl.no) (H.N. Ratliff), [Kyrre.Skjerdal@hvl.no](mailto:Kyrre.Skjerdal@hvl.no) (K. Skjerdal), [Ilker.Meric@hvl.no](mailto:Ilker.Meric@hvl.no) (I. Meric).<https://doi.org/10.1016/j.radphyschem.2025.112793>

Received 12 November 2024; Received in revised form 28 March 2025; Accepted 2 April 2025

Available online 10 April 2025

0969-806X/© 2025 The Authors. Published by Elsevier Ltd. This is an open access article under the CC BY license (<http://creativecommons.org/licenses/by/4.0/>).

following the annihilation of positrons emitted in  $\beta^+$  decay of neutron-deficient nuclei produced by nuclear interaction of ions (such as protons) with traversed tissue (Enghardt et al., 2004). However, the initial method suffers from physiological washout and counting statistics on orders of magnitude below conventional tracer imaging due to suboptimal instrumentation, which was prioritized for fast clinical translation rather than optimized for range verification. In response, in-beam PET scanners have been realized, tailoring PET imaging specifically for range verification to address these limitations (Bisogni et al., 2017; Yamaya et al., 2011). Additionally, some researchers are exploring the use of short-lived positron emitters produced during irradiation, such as  $^{12}\text{N}$ , to mitigate the inherent delay in conventional PET imaging and enhance its real-time applicability for proton therapy (Buitenhuis et al., 2017).

As an alternative to PET imaging for range verification, the detection of prompt gammas (PG), produced by inelastic interactions of protons with traversed tissue leaving target nuclei in an excited state to immediately emit (within nanoseconds) characteristic gamma rays, was suggested by Stichelbaut and Jongen (2003). Encouraged by initial measurements and Monte Carlo simulations of PG spatial distribution which showed strong correlation with dose delivery (Moteabbed et al., 2011; Polf et al., 2009), PGs have continued to be studied for the purpose of range verification and several systems have been proposed, including slit cameras (Bom et al., 2012; Smeets et al., 2012), prompt gamma timing (PGT) (Golnik et al., 2014), prompt gamma spectroscopy (PGS) (Verburg et al., 2013), and multistage Compton cameras (Hueso-González et al., 2016; Peterson et al., 2010). First clinical prototypes of measuring PG distributions in the patient are currently undergoing clinical studies (Berthold et al., 2021; Hueso-González et al., 2018).

While PG's use in range verification has been widely studied, recent research has explored the potential of secondary fast neutrons (FNs) for this purpose, with proposals including detection of neutron dose distributions (Marafini et al., 2017), proton recoil telescope setups for FN detection and range verification in proton therapy (Ytre-Hauge et al., 2019), and combined PG and thermal/epi-thermal neutron measurements with a pinhole camera (Lerendegui-Marco et al., 2022).

In the spring of 2023, the NOVO<sup>1</sup> consortium proposed a novel approach to real-time dose and range verification that is based on hybrid imaging of PGs and FNs emissions in proton therapy (Meriç et al., 2023) (for related work for see Turko et al. (2024), Ratliff et al. (2024), Schellhammer et al. (2023) and Setterdahl et al. (2024)). Beyond the clear benefit of increased statistical accuracy, PGs provide more detailed information about the beam's behavior near the Bragg peak, while FNs are primarily present in the entrance channel. Using both can offer insight into dose distribution for both targeted and surrounding tissues, helping to prevent the risks of over- or underexposure.

Designed to enhance the accuracy and safety of proton therapy, NOVO's proposed range verification system features a compact detector array (NOVCoDA) of modular detector elements. Each detector element comprises an organic plastic scintillator bar with dual-ended light readouts, housed in an aluminum casing for mechanical protection and light shielding. Ends of the scintillator are connected to dedicated readout electronics for signal processing. The modular design of the detector elements allows for flexible reconfiguration of their arrangement in the detector array to suit various experimental requirements. The NOVCoDA system is primarily intended for range monitoring of proton therapy beams, requiring high sensitivity to deviations in FN and PG production distributions along the beam axis. The detector has been purposefully designed to be compact, which significantly enhances its efficiency in detecting double FN scatters and triple PG interactions. The sensitive volume of the detector is composed of organic plastic scintillators. This material choice is crucial because plastic scintillators,

rich in hydrogen atoms, are highly effective at facilitating energy transfer from FNs and the primary interaction of gamma rays with energy ranging from 100 keV to 10 MeV is through Compton scattering.

The NOVCoDA functions by using PGs that interact three times (two consecutive Compton scatters and a third Compton scatter or photoabsorption) and FNs that elastically scatter on hydrogen nuclei, i.e.  $(n, p)$  scatter, twice in separate scintillator bars. A sketch of a triple PG interaction and double FN scatter is shown in Fig. 1.

For FNs, the scattered neutron energy  $E'_n$  can be determined by the time-of-flight (TOF) and distance  $d$  between the first and second scatter

$$E'_n = \frac{1}{2} m_n \left( \frac{d}{TOF} \right)^2, \quad m_n = 939.6 \text{ MeV}/c^2. \quad (1)$$

Energy transferred in the first  $(n, p)$  scatter can be estimated as the energy deposited in the scintillator bar by the recoil proton,  $E_p$ . As such, the initial neutron energy becomes  $E_n = E'_n + E_p$ , and the polar scattering angle,  $\theta$ , in the laboratory-frame, between the first scatter interaction and point of origin is derived by non-relativistic elastic scattering kinematics applying conservation of energy and momentum:

$$\theta = \sin^{-1} \sqrt{\frac{E_p}{E_n}}. \quad (2)$$

The azimuthal angle  $\phi$  of the first scatter remains unresolved such that  $\phi \in [0, 2\pi]$  and leads to the emergence of a cone-shaped surface, an object referred to as an event cone. An event cone (illustrated in Fig. 1) describes a set of coordinates from which the incident double-scattered FN (or triple-interaction PG) could have originated and is defined by its half-opening angle  $\theta$  (i.e., the polar scattering angle), the position vector of its vertex  $\mathbf{a} = [a_x, a_y, a_z]$ , and axis vector  $\mathbf{n} = [n_x, n_y, n_z]$ . The axis is defined as the unit vector connecting the second to the first particle interaction's position vector,  $\mathbf{s}_2$  and  $\mathbf{s}_1$  respectively, such that  $\mathbf{n} = \frac{\mathbf{s}_1 - \mathbf{s}_2}{\|\mathbf{s}_1 - \mathbf{s}_2\|}$ . Position vector of the vertex is defined as that of the first particle interaction,  $\mathbf{a} = \mathbf{s}_1$ .

Similar reconstruction of event cones can be performed for triple-interaction PGs for which  $\theta$  can be estimated using Compton collision kinematics. Reconstruction equations and methods for gamma rays will not be addressed in this paper, but are well-established in the literature (Dogan et al., 1990).

Acquiring multiple event cones allows for the reconstruction of the PG and FN production distributions within the patient. As changes in the proton beam range cause alterations in the production distributions of FNs and PGs, monitoring these alterations helps in detecting beam range deviations.

One of the factors influencing the overall quality of the reconstructed particle production distributions is the detector position resolution, which is determined by the constituent scintillators' depth-of-interaction (DOI) resolution and their short-end dimensions (width and height). The DOI resolution reflects the uncertainty in locating the particle interaction along the longitudinal axis of a scintillator. Spatial information regarding an interaction's coordinates in the cross-sectional plane in the short-end dimensions is compromised due to multiple optical photon scattering within large-aspect-ratio scintillator bars. As a best estimation, the particle interaction is assumed to occur at the bar's center in the cross-section plane, with an associated uniform uncertainty of half the bar's width and height in the corresponding dimensions. To improve position accuracy in these dimensions while maintaining the total scintillator volume per detector element, thinner bars could be arranged in a  $(2 \times 2)$  array, with each bar optically segmented to confine light production to the bar where particle scattering occurs. Optical segmentation can be achieved by leaving a small air gap between bars to allow scintillation light to undergo total internal reflection, and reflective paint/film such as polytetrafluoroethylene (PTFE), also known as Teflon, titanium dioxide paint, and ESR film can be applied to prevent light leakage between bars (Galindo-Tellez et al., 2021; Weinfurter et al., 2018).

Uncertainties in the interaction positions propagate to uncertainties in the parameters of constructed event cones. For FN event cones,

<sup>1</sup> NOVO: Next generation imaging for real-time dose verification enabling adaptive proton therapy.

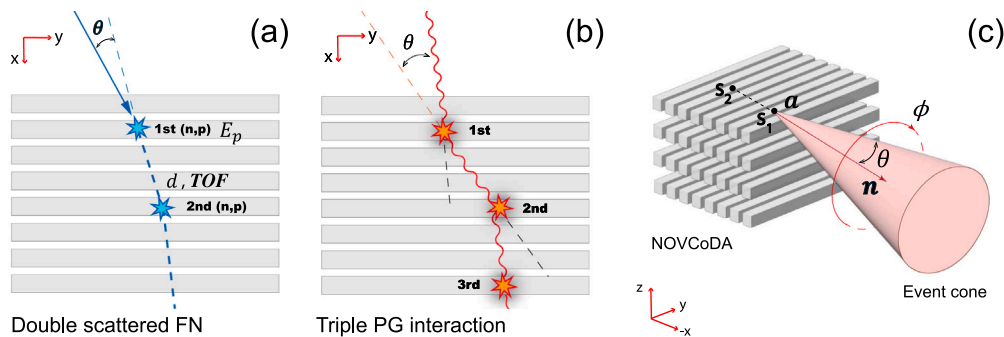


**Fig. 1.** To enable imaging of fast neutrons (FNs) and prompt-gamma rays (PGs) the NOVCoDA requires (a) double elastic scattering of FNs on hydrogen nuclei,  $(n, p)$ , and (b) triple PG interaction (two Compton scatters and a third Compton scatter or photoabsorption). The particle incident angle  $\theta$  can be constructed by elastic scattering kinematic and Compton collision kinematic equations for scattered FNs and interacting PGs, respectively, which yields an associated event cone characterized by its half-opening angle  $\theta$ , vertex  $a$ , and axis  $n$  — shown in (c). Event cones are used to reconstruct detected particles' production distributions.

the half-opening angle, Eq. (2), depends on the distance  $d$  between interaction points to estimate scattered FN energy, Eq. (1). The result of uncertainties in event cone parameters is reduced quality (e.g., spatial resolution) in reconstructions of particle production distributions. Additionally, the general quality of the reconstructed production distributions are further impacted by the orientation of the detector elements relative to the proton beam axis.

We denote unit vector of the proton beam axis as  $\mathbf{B}$  and define a line-of-sight (LoS) vector  $LoS$  as the unit vector orthogonal to the beam axis and parallel to the detector surface normal facing the beam axis (illustrated in Fig. 2). The simplest arrangement of detector elements is as a parallel array, which can be oriented in one of three ways: with detector elements longitudinal axis parallel to  $\mathbf{B}$  and perpendicular to  $LoS$ , perpendicular to both  $\mathbf{B}$  and  $LoS$ , and perpendicular to  $\mathbf{B}$  and parallel to  $LoS$ . These are later referred to as the “beam”, “upright”, and “LoS” orientation and are illustrated in Fig. 2.

Alternatively, the detector elements can be arranged in a woven-like array where layers alternate between detector elements being parallel and perpendicular to  $\mathbf{B}$ .

In this study, we investigate through Monte Carlo simulations the impact of detector element arrangement and scintillator position resolution on the proton-beam range shift determination capabilities of the NOVCoDA. As FNs have received less attention in proton range verification studies, we center our investigation on them. We evaluate two cases of scintillator position resolution, where the first considers detector elements with a single, monolithic  $1 \times 1 \times 14 \text{ cm}^3$  scintillator bars, while the other considers a quasi-monolithic  $1 \times 1 \times 14 \text{ cm}^3$  scintillator volume composed of  $0.5 \times 0.5 \times 14 \text{ cm}^3$  optically segmented scintillator bars arranged in a  $(2 \times 2)$  array, which effectively offers enhanced spatial resolution in two dimensions compared to the first case. We use minimum detectable range shift as a key indicator, representing the smallest shift in beam range (in mm) that the detector system can discern with a specified certainty for a given proton intensity. For example, at a beam intensity on the order of  $10^8$  protons per beam spot, the detector achieves a minimum detectable range shift of 1 mm. Details of this metric are provided in the methods section, Section 2. The structure of this paper is as follows: Section 2 describes the Monte Carlo simulations of FN production and detection, the explored detector arrangements, method of accounting for position resolutions in the scattering data, image reconstruction and estimating minimum detectable range shifts. Results are presented in Section 3. Limitations of our study and the practical challenges of optically segmented scintillator volumes is discussed in Section 4, and Section 5 concludes our work.

## 2. Methods

### 2.1. Monte Carlo simulations

The production and detection of FNs was modeled in the Monte-Carlo based simulation toolkit GATE (v.9.0) (Jan et al., 2004) with

Geant4 (v.10.6.3) (Allison et al., 2006; Agostinelli et al., 2003; Asai et al., 2016) using the QGSP\_BIC\_EMY physics list, the general recommendation for hadrontherapy simulations (Silva et al., 2020). The particle source and detector geometry were set up in a world of vacuum. The world frame of reference is denoted with  $(x, y, z)$ . To save simulation time and computational resources, simulations were split into two phases: neutron production and neutron detection.

The simulation setup for neutron production (Fig. 2a) involved a monoenergetic proton beam directed at a  $40 \times 50 \times 40 \text{ cm}^3$  homogeneous water phantom with geometrical center in  $(0, 10, 0) \text{ cm}$ . The proton beam was initialized with an energy of 85 MeV (corresponding to a 57.8 mm range in water (Berger et al., 1999)), a Gaussian profile where  $\sigma_x = \sigma_z = 2 \text{ mm}$ , and  $10^{10}$  primary protons. These values were selected to replicate typical clinical conditions, where therapeutic proton energies of 70–250 MeV (Mohan and Grosshans, 2017) are used and the Gaussian profile simulates standard beam spread. A realistic number of protons per beam spot lies in the range of  $10^6$  to  $10^{10}$  protons (Pausch et al., 2020). The choice of  $10^{10}$  protons in this work reflects the necessary particle statistics for achieving adequate reconstruction of production distributions and sensible range shift determination analysis. The proton beam's start was positioned at  $(0, -50, 0) \text{ cm}$  and assigned a momentum vector directed entirely along the positive  $y$ -axis, configured to strike the center of the phantom on the  $xz$ -plane. FNs produced within the phantom by the primary protons were stored in phase-space<sup>2</sup> files. A set of 11 simulations were executed where a layer of water was incrementally removed in steps of 1 mm from the phantom volume along the  $y$ -axis, parallel to the beam, resembling physical and/or anatomical changes (e.g., breathing motion or weight loss) in a patient that would result in a proton beam range to deviate from the expected/planned location. Neutron production simulations resulted in a set of 11 phase-space files, defining neutron sources for true range shift magnitudes ranging from 0 mm to 10 mm in steps of 1 mm.

Neutron detection was modeled utilizing the FN phase-space files from the initial proton-water interaction simulation as a neutron source. The setup is illustrated in Fig. 2b. A detector geometry was placed with its geometric center at  $(30, 0, 0) \text{ cm}$ , i.e., 30 cm from the beam axis. The water phantom from the initial neutron production simulations was not included in the neutron detection simulations to avoid neutron scattering and absorption within the phantom, again, to increase number of FNs scattering with the detector geometry. The rationale for and impact of removing the water phantom is further discussed in Section 4.

<sup>2</sup> The term “phase space” refers to the multidimensional space that describes the complete set of particle's physical properties at a given point in space, including both position and momentum.

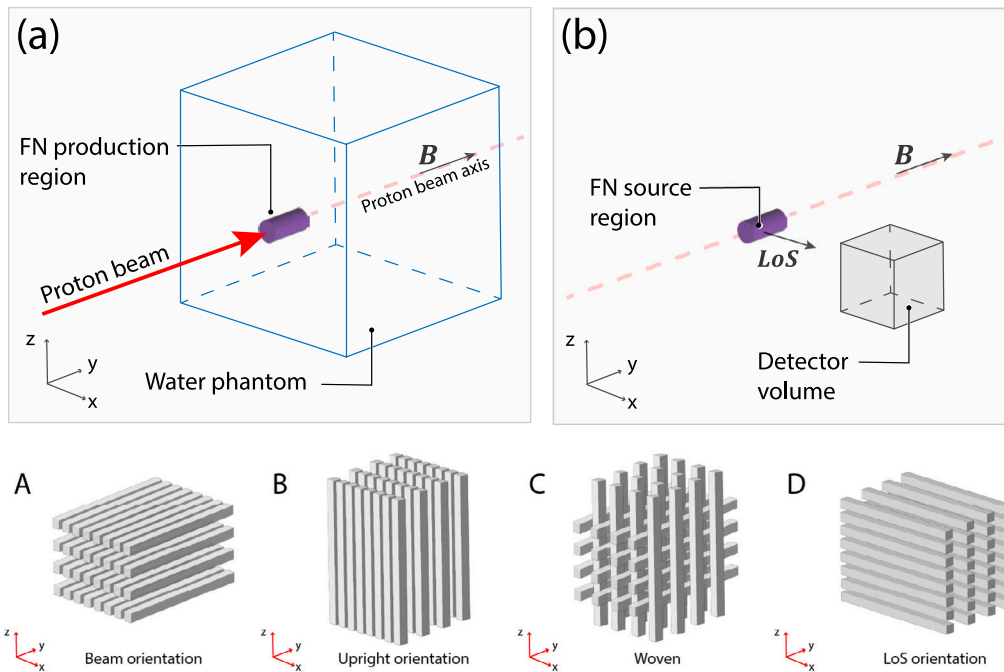


**Fig. 2.** Top: Simulation setup of (a) fast neutron (FN) production by an 85-MeV proton pencil beam in a  $40 \times 50 \times 40 \text{ cm}^3$  homogeneous water phantom and (b) FN detection within a detector geometry (represented by a cube). FNs produced in (a) are stored in phase-space files and used as a FN source in (b). Bottom: The four detector arrangements, used in FN detection simulations. FNs are produced by a proton beam with momentum parallel to the  $y$ -axis. Detector arrangements are referred to as (A) beam, (B) upright, (C) woven, and (D) LoS orientation. Where LoS refers to the line-of-sight unit vector that is perpendicular to the beam axis  $B$  and parallel to the normal vector of the detector surface facing  $B$ .

FNs scattering within the detector geometry were stored in ROOT files to be processed and used for subsequent event cone reconstruction.

A detector geometry consisted of an arbitrary number of thirty-two  $1 \times 1 \times 14 \text{ cm}^3$  plastic scintillator bars, organized into 8 layers with 4 bars in each layer, resulting in a total active detector volume of  $448 \text{ cm}^3$ . The spacing (center-to-center) between layers was set to 3 cm, and the spacing between scintillator bars within a layer was set to 1.5 cm. The material composition of the scintillator bars (with carbon-to-hydrogen atom ratio 10:11 and density  $1.099 \text{ g/cm}^3$ ) aligns with EJ-276 (Eljen Technology, 2020), which was originally considered for the NOVCoDA. However, other organic scintillator materials are now under examination. Four detector array arrangements (illustrated in Fig. 2) were investigated:

- (A) Beam oriented: the longitudinal axis of bars are oriented parallel to beam axis  $B$  and perpendicular to  $LoS$ .
- (B) Upright oriented: the longitudinal axis of bars are oriented perpendicular to beam axis  $B$  and perpendicular to  $LoS$ .
- (C) Woven: layers alternate between having bar orientations of (A) and (B).
- (D) LoS oriented: the longitudinal axis of bars are oriented perpendicular to beam axis  $B$  and parallel to  $LoS$ .

Eleven detector simulations, corresponding to the 11 beam ranges from the neutron production simulations, were performed for each detector arrangement.

## 2.2. Event processing

FN scatters in the detector geometry were processed using ROOT (v. 6.26) (Brun and Rademakers, 1997), a C++-based toolkit extensively used for the purpose of high processing efficiency and extensive data analysis.

FN event cones were reconstructed by requiring two consecutive elastic scatters with protons (hydrogen nuclei) in separate scintillator bars, each with an energy deposition of 100 keV or greater. Event cone

parameters were computed using Eq. (1) for the half-opening angle,  $a = s_1$  for the vertex, and  $n = \frac{s_1 - s_2}{\|s_1 - s_2\|}$  for the axis, where  $s_1$  and  $s_2$  represents the position vector of the first and second FN scatter. Event cone parameters were stored in ROOT files in list mode. Cones with an axis directed away from the neutron source (i.e.,  $a_x > 0$ ) were filtered out as these would not contribute to the reconstruction of the FN production distribution.

## 2.3. Incorporating position resolution

Two types of scintillator volumes were used in the various detector arrangements. These are shown in Fig. 3, and include (type 1) a monolithic volume of a  $1 \times 1 \times 14 \text{ cm}^3$  scintillator bar and (type 2) a quasi-monolithic  $1 \times 1 \times 14 \text{ cm}^3$  volume of a  $(2 \times 2)$  optically segmented array of  $0.5 \times 0.5 \times 14 \text{ cm}^3$  scintillator bars. The internal coordinate system of a scintillator volume is denoted with  $(x', y', z')$  (Fig. 3).

To isolate the effect of scintillator position resolution on reconstructed production distributions and range shift detection limits, perfect energy and timing resolutions were assumed, and only uncertainties in the position coordinates  $x'$ ,  $y'$ , and  $z'$  were accounted for in the FN scattering data.

FN scatter coordinates were assumed to occur at the center of a scintillator bar in the short-end dimensions. For the monolithic scintillator volume,  $(x', y') = (0, 0)$ . To emulate the quasi-monolithic scintillator volume of a  $(2 \times 2)$  array of optically segmented scintillators, scattering coordinates in the  $x'y'$ -plane were set to center of the simulated scintillator volume's quadrant the initial FN scatter was closest to. For example, a FN scatter occurring in the first quadrant of a scintillator volume would be assigned  $(x', y') = (0.25, 0.25) \text{ cm}$ , and one occurring in the third quadrant would be assigned  $(x', y') = (-0.25, -0.25) \text{ cm}$ , where 0.25 cm is one-fourth of the original bar width and height (1 cm).

A new  $z'$ -coordinate was randomly sampled from a Gaussian distribution centered at the initial  $z'$  scatter coordinate with a Full Width at Half Maximum (FWHM) of 10 mm, which corresponds to a typical value of an experimentally estimated DOI resolution for organic plastic scintillators (Turko et al., 2024; Sweany et al., 2019).

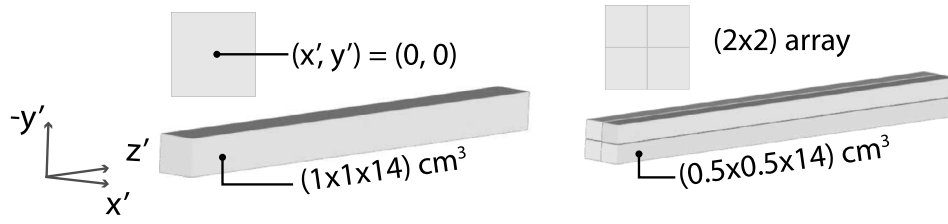


Fig. 3. Shown above are the two types of scintillator volumes used in the detector arrangements illustrated in Fig. 2. After neutron detection simulations, fast neutron (FN) scatters in a detector geometry are processed and event cones are assembled. Original neutron detection simulations utilized the scintillator volume on the left-hand side, a monolithic  $1 \times 1 \times 14 \text{ cm}^3$  scintillator bar. In processing FN scatters, a scintillator volume of thinner scintillator bars – resembling a  $(2 \times 2)$  array of optically segmented  $0.5 \times 0.5 \times 14 \text{ cm}^3$  scintillator bars – with corresponding position uncertainty on the  $x'y'$ -plane, was emulated by setting FN scatter coordinates to the center of the quadrant closest to the initial scatter location.

After updating  $(x', y', z')$  to account for scintillator position resolution, the new coordinates in the bar frame of reference were converted back to the world system and respective cone parameters for the modified double FN scatters were calculated.

#### 2.4. Image reconstruction

A virtual pixelized image plane, defined by the equation  $x = 0$  and bounded by  $y \in [-210, 200]$  mm and  $z \in [-200, 200]$  mm with  $1 \times 1 \text{ mm}^2$  pixels, was used to project event cones onto and reconstruct an image of the 2D production distribution of detected FNs by List-Mode Maximum Likelihood Expectation Maximization (LM-MLEM) (Barret et al., 1997; Wilderman et al., 1998b), one of the most prominent statistical methods applied to image reconstruction. The pixel-wise, update equation of LM-MLEM is

$$\lambda_j^{(k+1)} = \frac{\lambda_j^{(k)}}{s_j} \sum_i \frac{a_{ij}}{\sum_b a_{ib} \lambda_b^{(k)}} \quad (3)$$

in which  $\lambda_j^{(k)}$  is the value of pixel  $j$  at iteration  $k$ ;  $s_j$  is the sensitivity of pixel  $j$  and represents the probability of a particle emitted from said pixel being detected;  $I$  is the number of measured double-scattered FN events (i.e., the number of event cones);  $J$  is the number of pixels in the virtual image plane; and  $a_{ij}$  are elements of the system matrix, a large sparse matrix, in which row  $i$  represent the projection of event cone  $i$ . Rows of the system matrix are constructed on an event-by-event basis, and a unique system matrix must be computed for each new range shift measurement. The calculation of system matrix elements was based on a simplification of Wilderman's marching algorithm (Wilderman et al., 1998a). System matrix element  $a_{ij}$  was assigned a value of unity if event cone  $i$  intersected pixel  $j$  and was zero otherwise.

A flat image was used as an initial guess,  $\lambda_j^0 = 1 \forall j$ , and for simplicity, sensitivities were assumed equal to  $1 \forall j$ , meaning emission from all pixels are equally likely to be detected. Early stopping at an arbitrary predetermined iteration ( $k = 20$ ) was used to terminate the algorithm and prevent further noise enhancement in the updated image.

A signal region encompassing the high intensity region of the reconstructed FN distribution was defined, by eye, as  $y \in [-210, -60]$  mm and  $z \in [-50, 50]$  mm, corresponding to dimensions  $150 \times 100 \text{ mm}^2$ .

#### 2.5. Minimum detectable range shift

The procedure used for estimating range shift detection limits in terms of required proton intensities has been reported previously in Meric et al. (2023). We used the same procedure but with a few minor modifications, specifically how the longitudinal FN production profiles corresponding to different intensities were generated.

##### 2.5.1. Longitudinal profiles

One-dimensional histograms (longitudinal profiles) along the proton beam axis of the LM-MLEM reconstructed profiles in the signal region were created. Histogram bin widths equaled 1 mm. Bin weights were normalized such that sum of weights equaled unity,  $\sum_i w_i^* = 1$ , and  $w_i^*$  represents the relative probability of an emission coming from bin  $i$ .

Longitudinal profiles corresponding to different proton intensities were emulated by scaling normalized bin weights  $w_i^*$  with the ratio of desired proton intensity ( $N_{desired}$ ) to initial proton intensity ( $N_{initial} = 10^{10}$ ) multiplied by the number of event cones ( $N_{cones}$ ) observed in a range shift case. The weights  $w_i$  of these scaled profiles were computed with:

$$w_i = w_i^* \frac{N_{desired}}{N_{initial}} N_{cones}. \quad (4)$$

A set of longitudinal profiles was created corresponding to a number of desired proton intensities ranging from  $10^6$  to  $10^{10}$ . Fifteen discrete intensities were evenly sampled on a logarithmic scale between these two values.

##### 2.5.2. Range landmark

A range landmark (RL) metric, defined as the weighted average of histogram bins

( $\bar{x} = \frac{\sum_{i=1}^n w_i x_i}{\sum_{i=1}^n w_i}$ , where  $x_i$  is the value associated with the center or position and  $w_i$  is the weight of the  $i$ th bin), was computed for each longitudinal profile. Weights were normalized such that  $\sum_{i=1}^n w_i = 1$  before computing RLs.

In particle counting measurements, Poisson statistics are usually used to describe the expected variance of the data (Knoll, 2010). Mean and population standard deviation of a RL was computed using bootstrap resamples (Bruce et al., 2020). Weights  $w_i$  of longitudinal profiles, before normalization, were randomly sampled from a Poisson distribution with mean equal to the initial bin weight,  $\mu = w_i$ . Once a full new longitudinal profile was generated, weights were normalized and RLs computed. This was repeated for  $10^5$  iterations for all longitudinal profiles. The difference between a mean RL ( $\overline{RL}$ ) of a non-zero range shift and the  $\overline{RL}$  corresponding to a 0 mm shift is denoted as  $\Delta \overline{RL}$ .

##### 2.5.3. Range shift determination

Minimum detectable range shifts for a detector arrangement was estimated using a binary Gaussian Naïve Bayes (GNB) classifier. The implementation was done using python's scikit-learn library (Domingos and Pazzani, 1997). For each desired proton intensity, datasets of RL values corresponding to 0 mm and 1, ..., 10 mm true range shift magnitude, respectively labeled 0 ("no range shift") and 1 ("a range shift"), were assembled and used to train a GNB. For every range shift scenario, the GNB classifier underwent retraining and retesting on the same dataset for a fixed number of iterations ( $n = 1000$ ), with training (80%) and test (20%) sets being randomly chosen for each iteration. An average area under the receiver operating characteristic (AUROC) could then be computed. The detection limit in terms of

**Table 1**

Mean single FN scatter and double FN scatter observed over 11 range shifts of a proton beam with  $10^{10}$  primary protons for different detector arrangements and scintillator volume (scint. vol.) types, illustrated in Fig. 3. Type 1: monolithic scintillator volume, a  $1 \times 1 \times 14$  cm<sup>3</sup> bar. Type 2: A quasi-monolithic scintillator volume of an optically segmented ( $2 \times 2$ ) array of  $0.5 \times 0.5 \times 14$  cm<sup>3</sup> bars. Standard error (SE) of mean computed as  $SE = \sigma/\sqrt{n}$ , where  $\sigma$  is standard deviation over number of scatters observed in each range shifts measurement, and  $n = 11$  is the number of measurements.

Detector arrangement	Single FN scatter per proton ( $\cdot 10^{-6}$ )	Scint. vol. type	Double FN scatter per proton ( $\cdot 10^{-6}$ )
A Beam oriented	$341.87 \pm 0.12$	1	$4.2 \pm 0.009$
		2	$7.7 \pm 0.016$
B Upright oriented	$405.93 \pm 0.23$	1	$5.2 \pm 0.005$
		2	$9.4 \pm 0.013$
C Woven	$384.91 \pm 0.2$	1	$4.7 \pm 0.007$
		2	$8.0 \pm 0.014$
D LoS oriented	$363.26 \pm 0.12$	1	$3.7 \pm 0.012$
		2	$6.7 \pm 0.015$

proton intensity for a given range shift was determined based on a threshold of  $\overline{AUROC} \geq 0.9$ . Linear interpolation of  $\overline{AUROC}$  values was applied to achieve a more precise estimate of the necessary proton intensities. By repeatedly evaluating  $\overline{AUROC}$  as described, statistical uncertainties were estimated. These estimates were subsequently applied to determine the uncertainties in range shift detection limits related to the necessary proton intensities.

### 3. Results

#### 3.1. Fast neutron scatter efficiency

FN production caused by an 85-MeV proton beam in a homogeneous water phantom and detection in four different detector arrangements — i.e., (A) beam, (B) upright, (C) woven, and (D) LoS orientation — was simulated in GATE/Geant4. Two types of scintillator volumes were considered: (type 1) a monolithic volume of a  $1 \times 1 \times 14$  cm<sup>3</sup> scintillator bar and (type 2) a quasi-monolithic  $1 \times 1 \times 14$  cm<sup>3</sup> volume of a ( $2 \times 2$ ) optically segmented array of  $0.5 \times 0.5 \times 14$  cm<sup>3</sup> scintillator bars. Shifts in the proton beam were introduced by shaving off millimeters of the water phantom along the direction of the incident proton beam direction.

Average single and double scattering efficiencies over all range shifts for each detector arrangements and scintillator type are summarized in Table 1. The single scattering efficiency represents the number of single FN scatters depositing an energy of 100 keV or greater within the detector volume. The double scattering efficiency represents the number of FNs scattering at least twice within the detector volume, each scatter occurring in a separate scintillator bar. The double scattering efficiency reported in Table 1 represents the “useful” double FN scatter efficiency, meaning it includes only the events used for reconstruction of production distributions while excluding any invalid double scatter events (i.e., FN events whose corresponding event cone axis has a direction opposite of the simulated FN source,  $a_x > 0$ ). Both single and double scattering efficiency is reported in terms of number of scatters per simulated proton.

For all detector arrangements, the single scatter efficiency was on order of  $10^{-4}$  neutrons/proton, though the “upright” oriented parallel array (arrangement B) achieved the highest efficiency of  $4.06 \cdot 10^{-4}$  neutrons/proton and the other arrangements (A, C, and D), respectively achieved  $3.42 \cdot 10^{-4}$ ,  $3.85 \cdot 10^{-4}$ , and  $3.63 \cdot 10^{-4}$  neutrons/proton. In terms of double scatter efficiency, detector arrangements with the monolithic  $1 \times 1 \times 14$  cm<sup>3</sup> scintillator volume (type 1) demonstrated  $4.2 \cdot 10^{-6}$ ,  $5.2 \cdot 10^{-6}$ ,  $4.7 \cdot 10^{-6}$ , and  $3.7 \cdot 10^{-6}$  neutrons/proton for arrangement A, B, C, and D, respectively. When thinner scintillator bars,  $0.5 \times 0.5 \times 14$  cm<sup>3</sup>, clustered into ( $2 \times 2$ ) optically segmented  $1 \times 1 \times 14$  cm<sup>3</sup> scintillator

volumes (type 2) were used instead of the single  $1 \times 1 \times 14$  cm<sup>3</sup> bars (type 1), the double FN scatter efficiency roughly doubled, with an exception for arrangement D. Results indicate that the probability of a FN scattering more than once within the same volume is higher than it scattering in two unique, spatially separated, scintillator volumes. This was not the case for detector arrangement D due to the increased number of event cones with an axis pointing opposite (i.e.,  $a_x > 0$ ) of the known FN production direction from the detector’s field of view because of how DOI resolution is accounted for in the scattering data and how cones where  $a_x > 0$  are filtered out in the event processing stage. Double scatter efficiencies would have been nearly three times lower had the water phantom not been removed from the neutron transport calculations.

#### 3.2. Reconstruction of 2D and 1D fast neutron production profiles

Recall that the simulated proton beam was centered at  $z = 0$  and propagates along the  $y$ -axis. Two-dimensional (2D) FN production distributions were reconstructed in the  $yz$ -plane. A so-called one dimensional (longitudinal) profile represents the projection of a 2D FN production distributions onto the beam axis ( $y$ -axis).

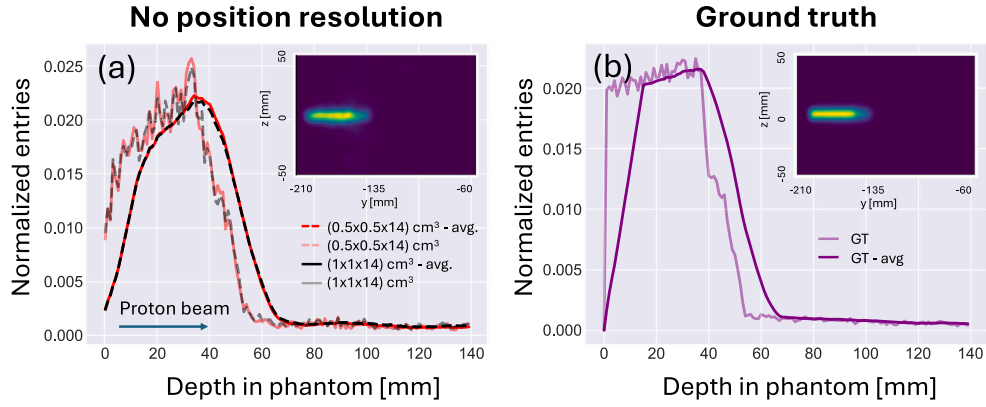
Fig. 4a presents the reconstructed FN production distribution for detector arrangement A for the 0 mm range shift scenario in the idealized case where detector position resolution effects are not considered. The corresponding ground truth FN production distribution, obtained from Monte Carlo simulations for the same detector arrangement, is shown in Fig. 4b. The ground truth FN production distribution is concentrated around the beam axis, with a slight spread along the  $z$ -axis of a few millimeters, due to the proton beam’s thickness. The no-resolution reconstructed longitudinal profile in Fig. 4a closely resembles that of the ground truth, with minor differences, such as a smoother rising and falling edge, which we attribute primarily to the reconstruction algorithm. Similarly shaped FN production distributions and longitudinal profiles were observed for the other detector arrangements and range shift scenarios.

Fig. 5 illustrates the reconstructed FN production distributions for the four detector arrangements and scintillator volume types in the 0 mm range shift scenarios and highlights the effect of detector position resolution associated with the monolithic (type 1) and optically segmented scintillator bars (type 2) on reconstructed distributions. Studying Fig. 5, it becomes apparent that detector position resolution degrades the spatial resolution of the reconstructed 2D FN production distributions, leading to “smearing” effects. Additionally, the arrangement of scintillator bars and the type of scintillator volume (type 1 or type 2) influence the nature of this effect. It can be seen that the use of optically segmented scintillator bars (type 2) generally reduces smearing in the 2D FN production distributions. Specifically, smearing is reduced along the  $z$ -direction for detector arrangements A and D and along the  $y$ -direction (beam axis) for arrangements B and C. The effect on reconstructions of arrangement B is particularly evident in the longitudinal profile, where the profile shape closely resembles that of the no-position-resolution case shown in Fig. 4a.

The “smearing” effect that is observed in reconstructed FN production distributions can be explained by the influence of detector position resolution on the uncertainties of event cone parameters used in the reconstruction, including the vertex, axis, and half-opening angle. When thinner scintillator bars are used, the improved position resolution in the short-end cross-section plane reduces uncertainties in these parameters, leading to less smearing and improved reconstruction quality. Implications of observed effects are discussed in Section 4.

#### 3.3. Linear correlation of estimated RLs and true range shifts

A mean range landmark ( $\overline{RL}$ ) over RLs of bootstrapped longitudinal profiles for all range shifts and proton intensities as well as the relative difference ( $\Delta RL$ ) of RLs to that of the true 0 mm range shift were



**Fig. 4.** One dimensional (longitudinal) profiles in signal region ( $y \in [-210, -60]$  mm and  $z \in [-50, 50]$  mm) of fast neutron (FN) production distribution caused by an 85-MeV proton beam interacting within a homogeneous water phantom as (a) reconstructed by LM-MLEM for scattering data observed by detector arrangement A with detector elements composed of either a monolithic  $1 \times 1 \times 14$  cm<sup>3</sup> scintillator bar (black) or a quasi-monolithic scintillator volume composed of a  $(2 \times 2)$  array of  $0.5 \times 0.5 \times 14$  cm<sup>3</sup> bars (red); and (b) from Monte-Carlo ground truth coordinates of detected double scatter events. Insert in (a) is the LM-MLEM reconstructed 2D production distribution with data obtained by arrangement A with a quasi-monolithic scintillator volume per detector element. .

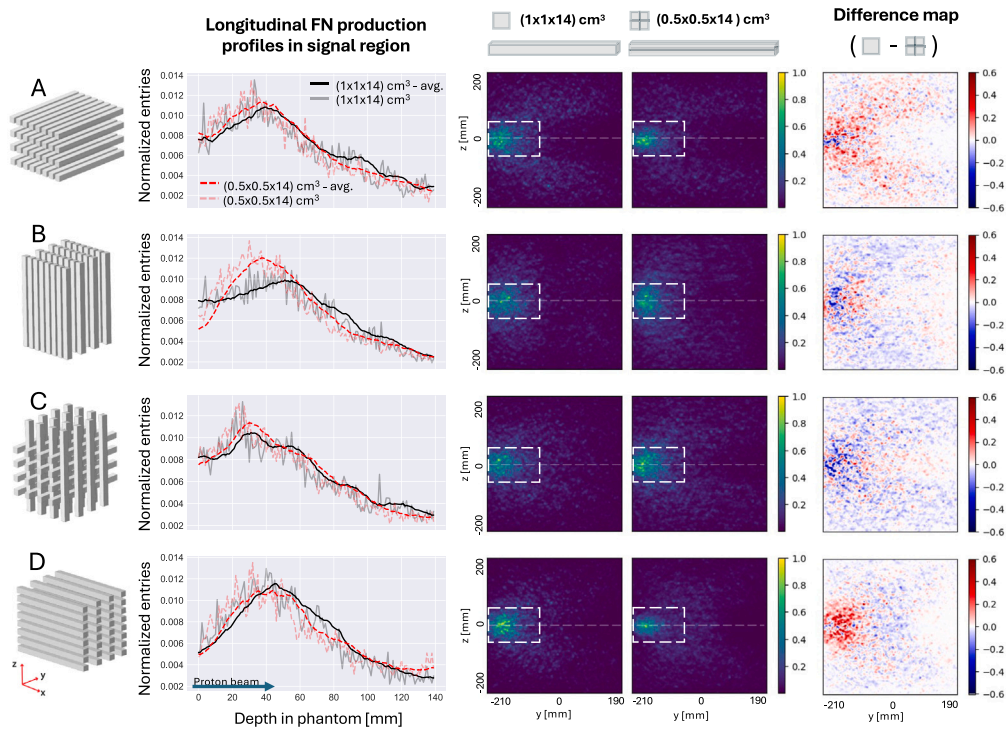


**Fig. 5.** Reconstructed two- and one-dimensional (longitudinal profile) fast neutron (FN) production distribution caused by an 85-MeV proton pencil beam (of  $10^{10}$  primary protons and momentum parallel to the  $y$ -axis) interacting in a homogeneous water phantom. A longitudinal profile is the projection onto the  $y$ -axis of the signal region (delineated by a white stippled rectangle) with  $y \in [-210, -60]$  and  $z \in [-50, 50]$  from the 2D distribution. Here, they are normalized such that the sum of bin weights = 1 and 2D distributions are normalized such that maximum pixel value is = 1. Reconstructed FN production distributions for four detector arrangements (A, B, C, and D) consisting of spatially separated bar-shaped scintillator volumes are shown in column 3 and 4. A multidimensional Gaussian filter with a standard deviation of 2 has been applied to the shown 2D production distributions to reduce noise and smooth pixel values in order to make the structures in the images discernible to the human eye. Two types of scintillator volumes are considered: (1) a monolithic  $1 \times 1 \times 14$  cm<sup>3</sup> bar and (2) a quasi-monolithic  $1 \times 1 \times 14$  cm<sup>3</sup> volume of a  $(2 \times 2)$  optically segmented array of  $0.5 \times 0.5 \times 14$  cm<sup>3</sup> bars. Detector position resolution is accounted for in reconstruction data by assuming FN scatters occur at the center of a scintillator bar's short-end cross section. The difference map shows the difference in the reconstructed 2D production distributions of detector arrangements with the first and second type of scintillator volume; red areas (positive values) and blue areas (negative values) indicate regions where FN signal is strongest in the respective reconstructions, and white regions indicate where the distributions take on the same relative intensities. The quasi-monolithic scintillator volume offers more precise position resolution. This is particularly reflected in the more clearly defined peak of longitudinal profile (dashed red line) of detector arrangement B and 2D distribution of arrangement D which is more concentrated about the beam axis.

found.  $\overline{\Delta RL}$  as a function of true range shift magnitude is shown in Fig. 6a and b for the monolithic (type 1) and quasi-monolithic (type 2) scintillator volumes, respectively, at a proton intensity of  $5.18 \cdot 10^9$  protons/spot. The figure demonstrates the linear correlation that is observed between shifts in the beam range and the reconstructed

distributions' RLs. Linear regression models were used to quantify the correlation between  $\overline{\Delta RL}$  and true range shift magnitudes. For all detector arrangements and types of scintillator volumes, regression models indicate a strong linear correlation ( $R^2 \geq 0.85$ ) in spite of fluctuations in the residuals, reflected in the lower panel of Fig. 6a

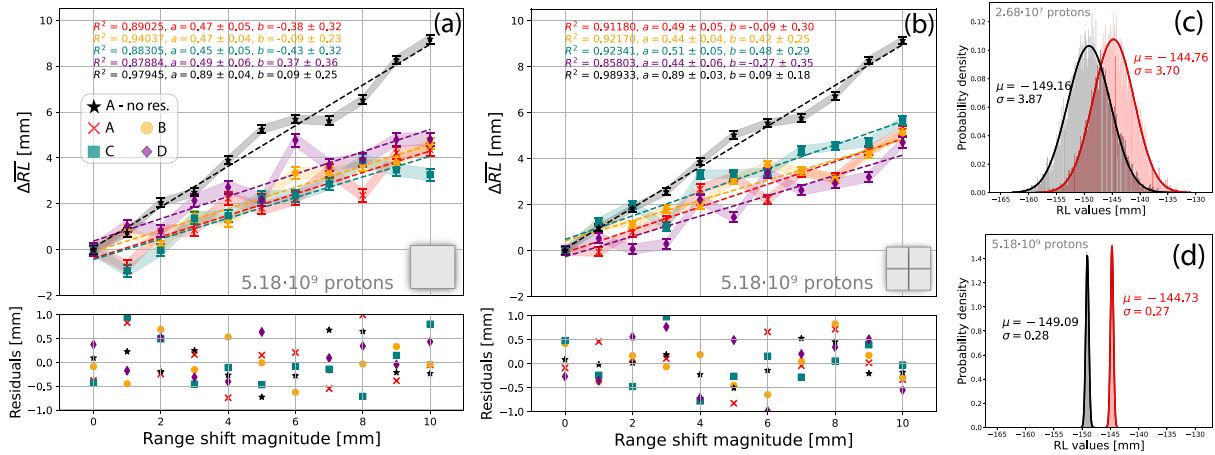


**Fig. 6.** The linear correlation between mean range landmark  $\overline{\Delta RL}$  and true range shift magnitude and residuals of detector arrangements with type 1 (a) and type 2 (b) scintillator volumes at a proton intensity of  $5.18 \cdot 10^9$  are shown in the top panels.  $\overline{\Delta RL}$  values corresponding to type 1 and 2 scintillator volumes without position resolution effects (no res.) of arrangement A are plotted with stippled black line for comparison. Range landmark (RL) distributions for detector arrangement A with type 1 scintillator, corresponding to 0 mm (black) and 10 mm (red) true range shifts, at a proton intensity of  $2.68 \cdot 10^7$  and  $5.18 \cdot 10^9$  are shown in (c) and (d), respectively. The distributions are fitted with a Gaussian, where  $\mu$  represents the mean and  $\sigma$  is the standard deviation.

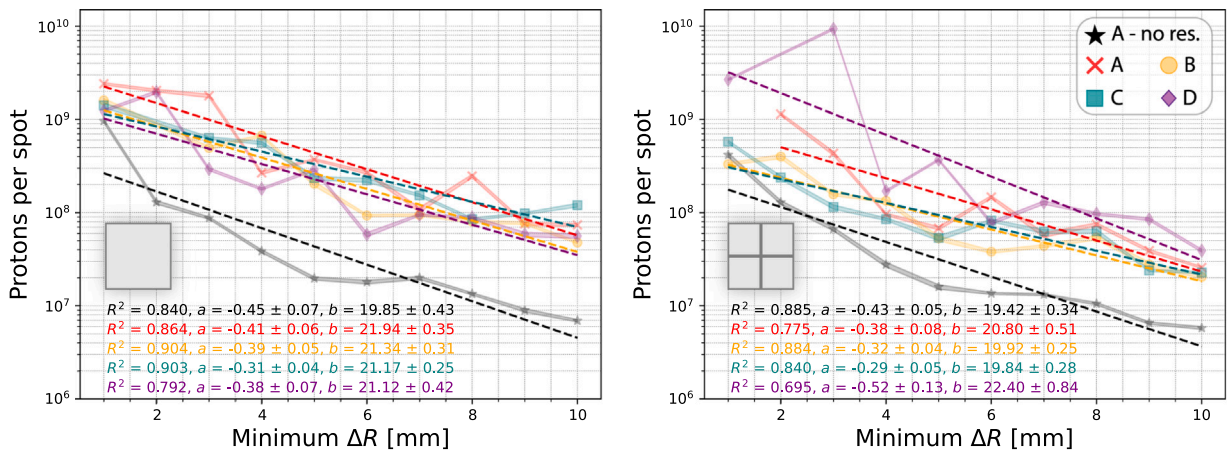


**Fig. 7.** Number of protons per spot as a function of minimum detectable range shift  $\Delta R$  for four detector arrangements and two types of scintillator volumes. Estimated proton intensities corresponding to detector arrangement A without position resolution effects (no res.) are plotted with stippled black line for comparison. Detection limits are significantly improved when an optically segmented type scintillator volume (right) is utilized.

and b.  $R^2$  values and regression parameters (slope  $a$  and intercept  $b$  in the linear model) were similar across all proton intensities, detector arrangements, and scintillator types.

Naturally, the standard error of  $\overline{\Delta RL}$ s is smaller at larger proton intensities as a result of increased event cone statistics. This is illustrated in Fig. 6c and d for the RL distributions corresponding to  $2.68 \cdot 10^7$  and  $5.18 \cdot 10^9$  protons. For the same reason, the standard error was smaller for  $\overline{\Delta RL}$ s corresponding to detector arrangements consisting of the type 2 scintillator volume composed of thinner  $0.5 \times 0.5 \times 14 \text{ cm}^3$  scintillator bars.

### 3.4. Detection limits

The impact of thinner scintillators on the detection capabilities of the NOVCoDA becomes evident when examining the detection limits, as shown in Fig. 7 in which the required proton intensity is shown as a function of minimum detectable range shift ( $\Delta R$ ). An expected inverse proportionality is observed, where fewer protons are required as the magnitude of range deviation increases. For the monolithic scintillator volume, the different detector arrangements show similar performance, with the ability to detect a 1 mm range shift at proton intensities with at least an order of  $10^9$  protons/spot, and a larger 10 mm shift at least an

order of  $10^7$  protons/spot. Where thinner scintillator bars are concerned (scintillator volume of type 2), the detector arrangements were capable of determining equivalent range shift magnitudes but at a significantly lower proton intensity. The exception is arrangement A, where the smallest discernible range shift magnitude was 2 mm. As shown in Fig. 6b, the estimated  $\overline{\Delta RL}$  values for 0 mm and 1 mm range shifts in detector arrangement A exhibit similar values and standard deviations ( $\sigma$ ), which reduces the separability of these distributions. This overlap poses a challenge for the trained GNB classifier to effectively distinguish between these shifts. A good example of improved detection limit resulting from the utilization of thinner bars (type 2) is that for detector arrangement B's where the estimated required proton intensity for identifying a 1 mm deviation in the proton beam range decreased from  $1.60 \cdot 10^9 \pm 5\%$  protons/spot to  $3.31 \cdot 10^8 \pm 3\%$  protons/spot, representing an improvement of 63% lower intensity. Over all minimum detectable range shifts, arrangement B with type 2 scintillator volumes requires on average 30% lower proton intensities than when the type 1, thicker, scintillator volumes are used. Detector arrangements A and C demonstrated similar improvements, respectively, requiring on average 60% and 67% lower proton intensity, while arrangement D requires on average 24% higher proton intensity.

## 4. Discussion

The results of this study underscore the potential for significant improvement in the NOVCoDA system's range shift determination performance through optimized detector arrangement. Additionally, the study highlights the impact of utilizing detector elements with optically segmented scintillator volumes, which reduces detector position resolution and enhances double FN scatter efficiency. Our findings indicate that employing thinner bars assembled in a  $(2 \times 2)$  optically segmented array per detector element, the system achieves roughly twice the double scatter efficiency (neutrons/proton) and at best, requires 63% fewer protons than the detector arrangements with the, not-optically segmented, monolithic scintillator volumes to discern a 1 mm range shift. We have also observed that detector arrangement influences the shape of the reconstructed 2D FN production distributions. While this may not directly pose a significant issue for range monitoring, where longitudinal profiles are primarily used, it could become a critical factor if the system is adapted for dose distribution monitoring where the 2D reconstructed production distribution might play a more central role.

In our work, we achieved a “useful” double FN scatter efficiency on order of  $10^{-6}$  neutrons/proton and a minimum detectable range shift of 1 mm at an estimated proton intensity on order of  $10^8$  protons/spot. Our results contrast with earlier work from the NOVO collaboration (Merici et al., 2023), where a double FN scatter efficiency of  $2.33 \cdot 10^{-4}$  neutrons/proton with less than 1% statistical uncertainty and a minimum detectable range shift of 1 mm at  $2.44 \cdot 10^7$  protons/spot was attained. Notably, their study used a CT-based phantom rather than a homogeneous water phantom and a single scatter volume for the detector geometry with dimensions  $30 \times 20 \times 20$  cm<sup>3</sup> and a total volume of 12 000 cm<sup>3</sup>, a substantially larger detector volume than what was considered in this work, making direct comparisons with our results challenging.

### 4.1. Rational for and impact of excluding the water phantom in neutron detection simulations

When neutron detection simulations are performed with a water phantom, neutrons generated within the phantom may undergo scattering before reaching the detector. This scattering results in both energy loss and a change in momentum, which can redirect neutrons away from the detector or reduce their energy below the 100 keV threshold required to detect double-scattered neutron events. Even when scattered neutrons retain enough energy to surpass the threshold, the reconstructed event cones will intersect the scattering position within the phantom, rather than the true neutron production site. As a result, the presence of a water phantom in neutron detection simulations, as described in Section 2.1, reduces double-scatter efficiency and introduces blurring in the reconstructed fast neutron (FN) distributions.

Two-dimensional reconstructions of FN production distributions were generated using a “naïve” LM-MLEM algorithm without regularization. Empirical trials applying the LM-MLEM algorithm, as described in this work, to double-scattered neutron data obtained from neutron detection simulations involving a water phantom and accounting for scintillator position resolution demonstrated that the algorithm was unable to produce images of sufficient quality for subsequent range shift determination analysis. This was primarily due to the lack of regularization, which led to difficulties in handling noise and the low efficiency of double neutron scattering.

To address these issues, we excluded the water phantom from subsequent neutron detection simulations. This allowed for LM-MLEM-based reconstructions and enabled us to focus solely on the effects of detector arrangements and scintillator position resolution on the reconstruction of 2D FN production distributions and the range shift detection capabilities of the NOVCoDA.

### 4.2. Study limitations

It is crucial to acknowledge that our study has limitations. The focus on FN alone does not fully encompass the NOVCoDA system's capability to detect both PGs and FNs. The absence of a water phantom in the FN detection simulations further limits our findings, as it does not account for neutron scattering and absorption within the phantom, nor does the study address the energy and time resolution of the detector. Consequently, the reported detection limits may not accurately reflect the NOVCoDA systems performance in a clinical setting.

It is important to note that DOI resolution is energy dependent and varies with different aspect ratio of plastic scintillators – as the dimensions of a bar effects the attenuation length  $\lambda$  of scintillation light, used in estimating the depth of interaction, e.g., as demonstrated in Sweany et al. (2019) – and with different plastic materials as they all have different attenuation lengths. In this work, we attribute the thicker  $1 \times 1 \times 14$  cm<sup>3</sup> and thinner  $0.5 \times 0.5 \times 14$  cm<sup>3</sup> scintillator bars the same DOI resolution, which may not accurately represent the actual DOI resolution of the latter due to a larger aspect ratio.

Future research should extend the analysis to include PG detection as well as the physical spacing between detector elements to determine ideal arrangements of NOVCoDA's detector elements to promote improved range detection limits. An extrapolation of the impact of detector element arrangement and detector position resolution on PG imaging, and PG and FN imaging combined, could provide valuable insight. Moreover, utilizing a regularized LM-MLEM algorithm capable of handling data generated under more realistic circumstances — e.g., using a CT-based phantom — and where all of the detector's resolutions (energy, time and position) are accounted for may offer further performance enhancements. Regularization could involve incorporating prior information on the expected particle (FN and PG) production distribution into the iterative update steps.

### 4.3. Practical challenges of optically segmented scintillator volumes

While the study highlights the benefits of optically segmenting scintillator volumes of detector elements in the NOVCoDA system, it is important to consider the associated challenges. The use of long, thin scintillator bars increases the risk of breakage and introduces potential issues such as optical crosstalk between segmented scintillator sections and electronical crosstalk among light readout channels. Moreover, high-energy recoil protons traveling between quadrants and being detected in both, registering as a false double-scatter pose further complications. Additionally, the increased number of readout channels necessitate more complex electronics and data acquisition systems, which could complicate the overall design. Therefore, further investigation is needed to address these challenges and evaluate the feasibility of implementing thinner bars in an optically segmented  $(2 \times 2)$  array within detector elements in practice.

### 4.4. Future directions for NOVCoDA testing and development

NOVO has planned several experimental campaigns to advance the development of the NOVCoDA system. Production of the aluminum housing and readout electronics is in progress and an assortment of organic scintillator bars of various materials (e.g., OGS and M600 provided by Sandia National Laboratories<sup>3</sup> and Target Systemechnik<sup>4</sup> respectively) and dimensions are at the NOVO consortium's disposal.

Up until now, less than a handful of miniature NOVCoDA demonstrators have been constructed and tested in experimental neutron

<sup>3</sup> Sandia National Laboratories, 7011 East Avenue, Livermore, CA 94550, U.S.A.

<sup>4</sup> Target Systemechnik GmbH & Co. KG, Heinz-Fangman-Straße, 42287 Wuppertal, Germany.

beamlines — not yet published. These NOVCoDA demonstrators have been assembled as an array of parallel detector elements (similar to arrangement A and B) and as an array of woven detector elements (similar to arrangement C). When comparing woven and parallel detector arrays, each design has distinct advantages and disadvantages. A woven detector array can reduce the distance between layers, allowing for a denser configuration and eliminating air gaps if widths of the electronic readout boards are optimized. It also offers better accessibility for cabling due to increased space between detector elements and readout units, facilitating easier connection and disconnection of cables. However, it poses challenges such as a larger footprint, more complex cabling, and difficulties accessing vertical detector elements for readout maintenance. In contrast, a parallel detector array is limited by the dimensions of the readout boards and photomultiplier tubes (PMTs), which dictate the minimum distance between layers, potentially leading to a less compact design. However, its configuration simplifies cabling logistics and allows for straightforward maintenance, albeit at the expense of space efficiency.

Thus far, experimental testing has utilized D–T generators as a neutron source at HZDR<sup>5</sup> and PTB<sup>6</sup> in Germany, which does not accurately represent the neutron production distribution found in proton therapy. Consequently, there has been limited focus on optimizing detector arrangement in favor of precise proton beam range shift detection. The primary objective has been to validate the NOVCoDA's capability to image neutron sources and detect their location. Looking ahead, future experimental campaigns will involve deploying the NOVCoDA in more clinically relevant settings, where the system will be exposed to both PGs and FNs generated by actual proton beams. In these scenarios, the arrangement of detector elements will be crucial, as it may introduce imaging artifacts that could impact detection limits. Based on the results presented in this work, both the woven detector arrangement (C) and the parallel “upright” detector arrangement (B) demonstrate comparable performance, making them both viable options; ultimately, the choice of arrangement will come down to practical considerations such as cabling, maintenance accessibility, and spatial constraints.

## 5. Conclusion

This study demonstrates the potential benefits of optimizing detector arrangement and employing optical segmentation of scintillator volumes of detector elements to enhance the performance of the NOVCoDA system in range shift determination for proton therapy. The NOVCoDA is designed for dual detection of prompt-gamma rays (PGs) and fast neutrons (FNs), however we limit our study to the latter. Our results indicate that using thinner, optically segmented scintillator bars nearly doubles the double scatter efficiency (neutrons/proton) and significantly improves range shift detection limits by reducing the required proton intensity by 30–60% when discerning a 1 mm range shift, which may significantly contribute to more accurate range verification and, consequently, better patient outcomes in clinical settings.

This study highlights that the “upright” oriented parallel array (detector element arrangement B) performs the best among tested arrangements, achieving the highest double FN scattering efficiency and the greatest detection limits of 1 mm at a beam intensity of  $3.31 \cdot 10^8$  protons/spot when optically segmented scintillator volumes are used for the detector elements. While this arrangement proves to be the most effective, the woven arrangement (C) also performs comparably in terms of mentioned metrics. Future studies should address, by simulation and experimental measurements, challenges such as scintillator fragility, optical and electronic crosstalk, and the complexity of electronic systems that comes with the utilization of optically segmented scintillator volumes.

Overall, this work provides a solid foundation for the continued development and optimization of the NOVCoDA system, with the goal of advancing its application in proton therapy and improving treatment precision and safety.

## CRedit authorship contribution statement

**Lena M. Setterdahl:** Writing – review & editing, Writing – original draft, Visualization, Software, Project administration, Methodology, Formal analysis, Data curation, Conceptualization. **William R.B. Lionheart:** Supervision. **Danny Lathouwers:** Writing – review & editing, Supervision, Methodology. **Hunter N. Ratliff:** Writing – review & editing, Supervision, Methodology. **Kyrre Skjerdal:** Writing – review & editing, Supervision, Methodology. **Ilker Meric:** Writing – review & editing, Supervision, Methodology, Funding acquisition.

## Declaration of competing interest

The authors declare that they have no known competing financial interests or personal relationships that could have appeared to influence the work reported in this paper.

## Acknowledgments

The NOVO project has received funding from the European Innovation Council (EIC)[1] under grant agreement No. 101130979. The EIC receives support from the European Union's Horizon Europe research and innovation program. Partners from The University of Manchester has received funding from UK Research and Innovation[2] under grant agreement No. 10102118. The authors acknowledge financial support by the Research Council of Norway[3] under the NANO2021 program (Grant No. 301459).

## Data availability

Data will be made available on request.

## References

- Agostinelli, S., et al., 2003. Geant4 – a simulation toolkit. *Nucl. Instrum. Methods A* 506 (3), 250–303. [http://dx.doi.org/10.1016/S0168-9002\(03\)01368-8](http://dx.doi.org/10.1016/S0168-9002(03)01368-8).
- Allison, J., et al., 2006. Geant4 developments and applications. *IEEE Trans. Nucl. Sci.* 53 (1), 270–278. <http://dx.doi.org/10.1109/TNS.2006.869826>.
- Asai, M., et al., 2016. Recent developments in Geant4. *Nucl. Instrum. Methods A* 835, 186–225. <http://dx.doi.org/10.1016/j.nima.2016.06.125>.
- Barret, H.H., et al., 1997. List-mode likelihood. *J. Opt. Soc. Am. A Opt. Image Sci. Vis.* 14 (11), 2914–2923. <http://dx.doi.org/10.1364/josaa.14.002914>.
- Berger, M., et al., 1999. ESTAR, PSTAR, and ASTAR: Computer programs for calculating stopping-power and range tables for electrons, protons, and helium ions (version 1.21). URL <http://physics.nist.gov/Star>.
- Berthold, J., et al., 2021. First-in-human validation of CT-based proton range prediction using prompt gamma imaging in prostate cancer treatments. *Int. J. Radiat. Oncol. Biol. Phys.* 111 (4), 1033–1043. <http://dx.doi.org/10.1016/j.ijrobp.2021.06.036>.
- Bisogni, M.G., et al., 2017. INSIDE in-beam positron emission tomography system for particle range monitoring in hadrontherapy. *J. Med. Imaging* 4, 011005. <http://dx.doi.org/10.1117/1.JMI.4.1.011005>.
- Bom, V., et al., 2012. Real-time prompt gamma monitoring in spot-scanning proton therapy using imaging through a knife-edge-shaped slit. *Phys. Med. Biol.* 57, 297–308. <http://dx.doi.org/10.1088/0031-9155/57/2/297>.
- Bruce, P., et al., 2020. *Practical Statistics for Data Scientists*, second ed. O'Reilly Media, Inc..
- Brun, R., Rademakers, F., 1997. ROOT – An object oriented data analysis framework. *Nucl. Instrum. Methods A* 389, 81–86. [http://dx.doi.org/10.1016/S0168-9002\(97\)00048-X](http://dx.doi.org/10.1016/S0168-9002(97)00048-X). URL <http://root.cern.ch/>, Proceedings of AIHENP'96 Workshop, Lausanne, Sep 1996.
- Buitenhuis, H., et al., 2017. Beam-on imaging of short-lived positron emitters during proton therapy. *Phys. Med. Biol.* 62, 4654–4672. <http://dx.doi.org/10.1088/1361-6560/aa6b8c>.
- Dogan, N., et al., 1990. Multiple Compton scattering gamma ray imaging camera. *Nucl. Instrum. Methods A* 299 (1), 501–506. [http://dx.doi.org/10.1016/0168-9002\(90\)90832-Q](http://dx.doi.org/10.1016/0168-9002(90)90832-Q).

<sup>5</sup> HZDR: Helmholtz-Zentrum Dresden-Rossendorf.

<sup>6</sup> PTB: Physikalisch-Technische Bundesanstalt.

- Domingos, P., Pazzani, M., 1997. On the optimality of the simple Bayesian classifier under zero-one loss. *Mach. Learn.* 29, 103–130. <http://dx.doi.org/10.1023/A:1007413511361>.
- Eljen Technology, 2020. EJ-276 datasheet. URL <https://eljentechnology.com/products/plastic-scintillators/ej-276>.
- Enghardt, W., et al., 2004. Charged hadron tumour therapy monitoring by means of PET. *Nucl. Instrum. Methods A* 525, 284–288. <http://dx.doi.org/10.1016/j.nima.2004.03.128>.
- Fredriksson, A., et al., 2011. Minimax optimization for handling range and setup uncertainties in proton therapy. *Med. Phys.* 38 (3), 1672–1684. <http://dx.doi.org/10.1118/1.3556559>.
- Galindo-Tellez, A., et al., 2021. Design and calibration of an optically segmented single volume scatter camera for neutron imaging. *J. Instrum.* 16 (4), P04013. <http://dx.doi.org/10.1088/1748-0221/16/04/P04013>.
- Golnik, C., et al., 2014. Range assessment in particle therapy based on prompt gamma-ray timing measurements. *Phys. Med. Biol.* 59, 5399–5422. <http://dx.doi.org/10.1088/0031-9155/59/17/5399>.
- Hueso-González, F., et al., 2016. Compton camera and prompt gamma ray timing: Two methods for in vivo range assessment in proton therapy. *Front. Oncol.* 6, 56. <http://dx.doi.org/10.3389/fonc.2016.00080>.
- Hueso-González, F., et al., 2018. A full-scale clinical prototype for proton range verification using prompt gamma-ray spectroscopy. *Phys. Med. Biol.* 63 (18), 185019. <http://dx.doi.org/10.1088/1361-6560/aad513>.
- Jan, S., et al., 2004. GATE: a simulation toolkit for PET and SPECT. *Phys. Med. Biol.* 49 (19), 4543–4561. <http://dx.doi.org/10.1088/0031-9155/49/19/007>.
- Knoll, G.F., 2010. *Radiation Detection and Measurement*, fourth ed. Wiley, New York, NY.
- Lerendegui-Marco, J., et al., 2022. Simultaneous neutron and gamma imaging system for real-time range and dose monitoring in hadron therapy and nuclear security applications. In: *EPJ Web Conf.* Vol. 261, EDP Sciences, p. 05001. <http://dx.doi.org/10.1051/epjconf/202226105001>.
- Marafini, M., et al., 2017. MONDO: A neutron tracker for particle therapy secondary emission characterisation. *Phys. Med. Biol.* 62, 3299–3312. <http://dx.doi.org/10.1088/1361-6560/aa623a>.
- Meric, I., et al., 2023. A hybrid multi-particle approach to range assessment-based treatment verification in particle therapy. *Sci. Rep.* 13 (1), 6709. <http://dx.doi.org/10.1038/s41598-023-33777-w>.
- Mohan, R., Grosshans, D., 2017. Proton Therapy - present and future. *Adv. Drug Deliv. Rev.* 109, 26–44. <http://dx.doi.org/10.1016/j.addr.2016.11.006>.
- Moteabbed, M., et al., 2011. Monte Carlo patient study on the comparison of prompt gamma and PET imaging for range verification in proton therapy. *Phys. Med. Biol.* 56, 1063–1082. <http://dx.doi.org/10.1088/0031-9155/56/4/003>.
- Paganetti, H., 2012. Range uncertainties in proton therapy and the role of Monte Carlo simulations. *Phys. Med. Biol.* 57, R99–R117. <http://dx.doi.org/10.1088/0031-9155/57/11/R99>.
- Particle Therapy Co-Operative Group (PTCOG), 2022. Patient statistics. <https://www.ptcog.site/index.php/patient-statistics-2>. (Accessed 16 September 2024).
- Pausch, G., et al., 2020. Detection systems for range monitoring in proton therapy: Needs and challenges. *Nucl. Instrum. Methods A* 954, 161227. <http://dx.doi.org/10.1016/j.nima.2018.09.062>.
- Peterson, S.W., et al., 2010. Optimizing a three-stage Compton camera for measuring prompt gamma rays emitted during proton radiotherapy. *Phys. Med. Biol.* 55, 6841–6856. <http://dx.doi.org/10.1088/0031-9155/55/22/007>.
- Petit, S., et al., 2013. Increasing maximum tumor dose to manage range uncertainties in IMPT treatment planning. *Phys. Med. Biol.* 58 (20), 7329–7346. <http://dx.doi.org/10.1088/0031-9155/58/20/7329>.
- Polf, J., et al., 2009. Prompt gamma-ray emission from biological tissues during proton irradiation: a preliminary study. *Phys. Med. Biol.* 54, 731–743. <http://dx.doi.org/10.1088/0031-9155/54/3/002>.
- Ratliff, H.N., et al., 2024. The backscatter gating method for time, energy, and position resolution characterization of long form factor organic scintillators. *J. Instrum.* 19 (07), P07002. <http://dx.doi.org/10.1088/1748-0221/19/07/P07002>.
- Schellhammer, S.M., et al., 2023. Hybrid treatment verification based on prompt gamma rays and fast neutrons: multivariate modelling for proton range determination. *Front. Phys.* 11, <http://dx.doi.org/10.3389/fphy.2023.1295157>.
- Setterdahl, L.M., et al., 2024. Image reconstruction for proton therapy range verification via U-NETs. In: Yap, M.H., Kendrick, C., Behera, A., Cootes, T., Zwiggelaar, R. (Eds.), *Medical Image Understanding and Analysis*. Springer Nature Switzerland, pp. 232–244. [http://dx.doi.org/10.1007/978-3-031-66955-2\\_16](http://dx.doi.org/10.1007/978-3-031-66955-2_16).
- Silva, R., et al., 2020. GEANT4 simulation in proton medical imaging: A transport models comparison. *Radiat. Phys. Chem.* 172, 108814. <http://dx.doi.org/10.1016/j.radphyschem.2020.108814>.
- Smeets, J., et al., 2012. Prompt gamma imaging with a slit camera for real-time range control in proton therapy. *Phys. Med. Biol.* 57, 3371–3405. <http://dx.doi.org/10.1088/0031-9155/57/10/3371>.
- Stichelbaut, F., Jongen, Y., 2003. Presented at the PTCOG 39. San Francisco.
- Sweany, M., et al., 2019. Interaction position, time, and energy resolution in organic scintillator bars with dual-ended readout. *Nucl. Instrum. Methods A* 927, 451–462. <http://dx.doi.org/10.1016/j.nima.2019.02.063>.
- Tattenberg, S., et al., 2021. Proton range uncertainty reduction benefits for skull base tumors in terms of normal tissue complication probability (NTCP) and healthy tissue doses. *Med. Phys.* 48, 5356–5366. <http://dx.doi.org/10.1002/mp.15023>.
- Tattenberg, S., et al., 2022. Range uncertainty reductions in proton therapy may lead to the feasibility of novel beam arrangements which improve organ-at-risk sparing. *Med. Phys.* 49, 4693–4704. <http://dx.doi.org/10.1002/mp.15766>.
- Turko, J., et al., 2024. Characterization of organic glass scintillator bars and their potential for a hybrid neutron/gamma ray imaging system for proton radiotherapy range verification. *J. Instrum.* 19, P01008. <http://dx.doi.org/10.1088/1748-0221/19/01/P01008>.
- Verburg, J.M., et al., 2013. Energy- and time-resolved detection of prompt gamma-rays for proton range verification. *Phys. Med. Biol.* 58, L37–L49. <http://dx.doi.org/10.1088/0031-9155/58/9/L37>.
- Weinfurther, K., et al., 2018. Model-based design evaluation of a compact, high-efficiency neutron scatter camera. *Nucl. Instrum. Methods A* 883, 115–135. <http://dx.doi.org/10.1016/j.nima.2017.11.025>.
- Wilderman, S., et al., 1998a. Fast algorithm for list mode back-projection of Compton scatter camera data. *IEEE Trans. Nucl. Sci.* 45 (3), 957–962. <http://dx.doi.org/10.1109/23.682685>.
- Wilderman, S., et al., 1998b. List-mode maximum likelihood reconstruction of Compton scatter camera images in nuclear medicine. In: *IEEE Nucl Sci Symp Conf Rec.* Vol. 3, pp. 1716–1720. <http://dx.doi.org/10.1109/NSSMIC.1998.773871>.
- Yamaya, T., et al., 2011. Development of a small prototype for a proof-of-concept of OpenPET imaging. *Phys. Med. Biol.* 56, 1123–1137. <http://dx.doi.org/10.1088/0031-9155/56/4/007>.
- Yock, A.D., et al., 2019. Robustness analysis for external beam radiation therapy treatment plans: Describing uncertainty scenarios and reporting their dosimetric consequences. *Pr. Radiat. Oncol.* 9 (4), 200–207. <http://dx.doi.org/10.1016/j.prro.2018.12.002>.
- Ytre-Hauge, K.S., et al., 2019. A Monte Carlo feasibility study for neutron based real-time range verification in proton therapy. *Sci. Rep.* 9, 2011. <http://dx.doi.org/10.1038/s41598-018-38384-6>.